**Program Digest, 2019 IEEE International Ultrasonics Symposium (IUS)**
**Glasgow, Scotland, October 6-9, 2019**

# B-mode and Doppler imaging of in vivo rat brain and ex vivo human brain with a high frequency endoscopic phased array

Thomas G. Landry
*Department of Surgery,*
*Nova Scotia Health Authority*
Halifax, Canada
tglandry@dal.ca

Jeremy A. Brown
*Biomedical, Electrical Engineering,*
*Dalhousie University*
Halifax, Canada
j.brown@dal.ca

***Abstract*—A high frequency ultrasound endoscope could find applications in many fields of surgery and diagnostics. Our group has been developing phased array endoscopes in the 30-45 MHz range, along with beamforming hardware for high resolution imaging, with a focus on neurosurgical applications. In this study, we imaged in vivo anesthetized rat brains and ex vivo human brain samples in order to characterize brain tissue appearance. A simple blood flow imaging method was also used in vivo to view some of the vasculature. Imaged brain tissue was sectioned and stained for comparison with the ultrasound images. In vivo, we found that the fluid-filled ventricles and boundaries between adjacent tissue regions separated by fissures were the most distinct features. Other brain substructures were also visible, such as the granular cell layers of hippocampus, caudate putamen, and cerebellar layers. In rats, gray matter and white matter did not appear as different as expected. However, in human brain samples the cerebral gray/white matter distinction was more obvious.***

***Keywords*—high frequency ultrasound, brain imaging, neurosurgery, endoscope, cerebral blood flow***

## I. Introduction

Traditional endoscopic surgery allows surgeons to perform procedures with minimal invasiveness, reducing the risk of complications and accelerating recovery. However, its usefulness is dependent upon maintaining an optical path free of blood and obscuring structures, and the imaging is limited to the visual surface. Our group has developed a high-frequency ultrasound (HFUS) imaging endoscope to address these limitations [1]. Ultrasound can penetrate most biological tissues, so an obscured view is much less of a problem, and structures beneath the surface can also be imaged.

In neurosurgery, procedures are generally preceded by noninvasive brain imaging such as magnetic resonance imaging not only to assess a pathology, but also to view the general anatomy to formulate a "road map" for the procedure. However, the intraoperative brain anatomy becomes significantly distorted relative to the preoperative scan [2]. Therefore, a HFUS endoscope could be very useful for neurosurgical endoscopy, allowing real-time depth-penetrating imaging. Furthermore, the additional imaging modes that ultrasound is capable of, such as blood flow imaging and elastography, would provide an entirely new suite of intraoperative diagnostic and assessment tools.

## II. Methods

### A. Imaging system

Phased array devices were built using previously described methods [1], [3]. Briefly, Cu was deposited on PZT5H piezoelectric substrate and 64 electrode patterns with 38 μm pitch were generated using photolithography. The material was lapped to 48 μm thickness (40-45 MHz resonance). Mechanical dicing was done from the back side to provide some mechanical isolation between elements. Ground electrode and wires were attached to the back face and alumina-loaded 301 epoxy was deposited as a backing layer. The array electrodes were wire bonded to flexible printed circuit boards that connected to a cabling system. A parylene and Cu mass-spring matching layer was then deposited [3], plus a quarter-wavelength parylene matching layer. An acoustic lens of epoxy resin was then cast onto the endoscope face to create an elevation focus at 7 mm. The packaged endoscope tip size was less than 4×4 mm.

For imaging, a 64 channel beamformer, built in-house, was used with custom software written in Python. The imaging sector window was 8 mm wide, covering 2-10 mm depth from the endoscope face with 128 imaging angle lines. Four transmit focal zones were used for each angle/line, and each line was sampled twice in succession (100 μs interval) before capturing the next angle. During imaging, the data from the two line-pairs were averaged at depth to reduce noise. Other image processing methods were used to improve image quality, including bandpass filtering, exponentially weighted moving averaging across frames, and edge enhancement.

Blood flow was displayed as a power Doppler image from the angle line pair differences. Therefore, only speckle that was changing by a significant amount within the 100 μs line pair interval was detectable. The power Doppler data, with optional

averaging across multiple frames, was overlaid in color onto the B-mode imaging data in real-time.

In some experiments, the tissue was also imaged with a commercially available linear array HFUS system (Vevo 2100, VisualSonics Inc., Toronto, Canada) for comparison, and to view with a larger imaging window. However, all presentation of HFUS imaging results pertains to imaging with the endoscope system unless stated otherwise. All imaging was performed with ultrasound gel as a coupling medium.

### *B. In vivo rat brain imaging*

All procedures were approved by the Dalhousie University Committee on Laboratory Animals. Rats (n = 14, young adult male Wistar) were anesthetized with isoflurane in $O_2$ and the head was placed in a stereotaxic frame. A craniotomy was drilled over the right side of the brain from 1.0-1.5 mm left of midline to the right edge of the skull (4-6 mm total width). This width usually extended anteriorly from the skull reference point bregma (*B*) +4.5 mm to *B*−14.5 mm (posterior skull edge) in order to allow imaging of most of the right hemisphere, including midline (n = 9). In some animals (n = 5), smaller craniotomy windows as small as 1.5×5.0 mm were used in one or two locations rather than the large window above. Almost all imaging was performed with the dura mater intact, as an early experiment found that removing the dura had little to no effect on image quality.

Following imaging, rats were sacrificed with an overdose of sodium pentobarbital, then transcardially perfused with 37°C phosphate-buffered saline followed by 4°C neutral buffered formalin. The brain was extracted and post-fixed in 4°C formalin overnight.

### *C. Ex vivo human brain samples*

Whole unfixed post-mortem brain hemispheres from Alzheimer's disease patients (n = 2) were obtained frozen with the dura mater in tact from the Maritime Brain Tissue Bank. Although there are microscopic differences between normal and Alzheimer's brains [4], these would not be expected to affect the gross anatomical imaging performed in this study.

### *D. Histology and data analysis*

For rat brains, the fixed tissue was razor cut into slabs 2-4 mm thick along a slice plane used during HFUS imaging (sagittal or coronal). Slabs were sunk in 15% sucrose, then sunk in 30% sucrose, then placed in a 3:1 mixture of 30% sucrose and O.C.T. cryoembedding medium for several hours. The slabs were then cryoembedded in O.C.T. and 35 µm thick sections were cut with a cryostat. Slides were air dried for two days then stained with hematoxylin and eosin (H&E). The gross anatomy was examined with low magnification. A rat brain atlas was used as an anatomical reference guide [5].

In some cases, structures were directly compared between H&E sections and HFUS images by tracing lines on the H&E image in Inkscape software, then overlaying those lines on the corresponding HFUS image. Some minor distortion of the original lines was allowed for differences resulting from intracranial pressure in vivo and tissue changes from fixation, and for slight differences in imaging/sectioning angle. The HFUS B-mode grayscale contrast between select brain structures was determined in some animals. The mean value of a representative region of each structure was calculated, and the absolute difference was divided by 255. The contrast was then pooled across animals for each structure comparison.

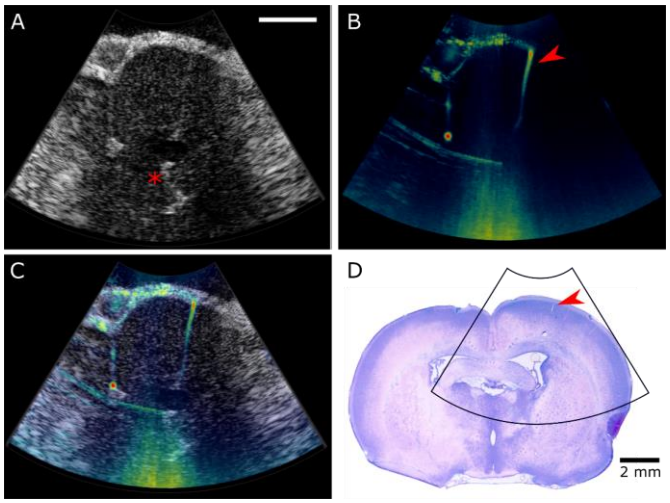


Fig. 1. A) In vivo rat brain coronal B-mode image at *B*−1.0 mm illustrating how abutted surfaces (e.g. *) appeared brighter than those opening into ventricle space (dark spot above *). B) Blood flow image from the same data (150 averages). A cortical blood vessel is highlighted (arrowhead). C) Combined B-mode and blood flow data. D) H&E stained section of the same region. A blood vessel was seen in the same location as in the blood flow data.

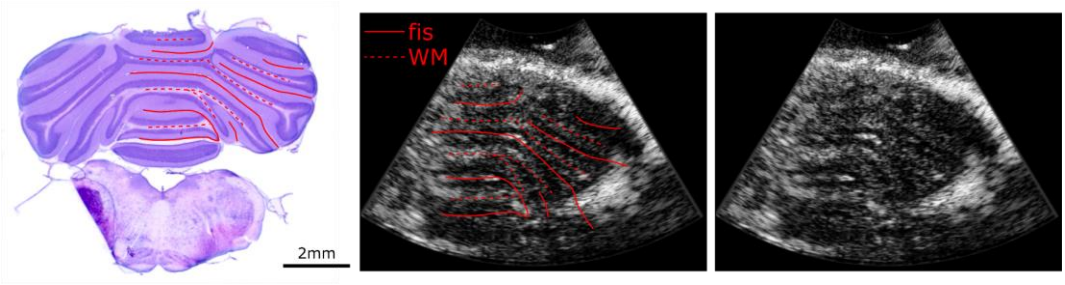


Fig. 2. In vivo rat brain coronal B-mode image at *B*−14.0 mm (right) showing the cerebellar layers. In the corresponding H&E section (left) the cerebellar fissures (fis, solid lines) and white matter (WM, dashed lines) paths were traced. These were overlaid on the B-mode image, showing good agreement with B-mode features. Note that the brighter features following the dashed lines are not necessarily the white matter itself, as associated molecular and granular cell layers also follow the same path. Indeed, the spatial relationships indicate the bright bands around the dashed lines are the granular cell layers and the adjacent dark bands are molecular cell layers (dark purple and medium purple layers, respectively, in the H&E image), with the white matter layer not clearly visible in this case. Sometimes the white matter was somewhat visible as a darker band within the granular cell layer in other animals (e.g. cerebellum example in Fig.4).

## III. Results

Some consistent observations were made across the rat brains. The features that were most distinct within the brain were the boundaries of tissue surfaces. This included not only the contrast between brain tissue and cerebrospinal fluid spaces of the ventricles (e.g. Fig.1), but also when the surfaces were fully abutted with another tissue surface. In fact, abutted tissue surfaces often had greater contrast with the tissue bulk than surfaces next to open fluid space, and even between the bulk and the fluid space itself.

For example, the open anterodorsal region of lateral ventricle (around *B*−1.0 mm) was visible as a dark area, but with no significant increase in brightness at the boundary itself, whereas in the area ventral to this, where the fornix abuts the caudate putamen, the boundary appeared bright (Fig.1). The cerebellar fissures, which are also effectively closed by the abutting cerebellar lobules, were also bright (Fig.2). Tighter, nearly fused fissures such as the hippocampal fissure, were often visible, but less prominently (Fig.3).

Some brain substructures were visible in HFUS images. The molecular layers versus granular layers of the cerebellum were particularly distinct, with the molecular layers being darker than the granular layers (Fig.2). The hippocampal molecular and granular layers were also consistently distinct (Fig.3), though the contrast was less than in the cerebellum. The caudate putamen also appeared darker compared to the overlying neocortex. Contrast analysis results are shown in Fig. 4.

Given that brain white matter has a much larger proportion of fatty myelin than gray matter, and largely consists of aligned neural fibers, we expected white matter/gray matter boundaries to be one of the most distinct features in the brain. However, in rat brains, the corpus callosum and cerebellar white matter tracts

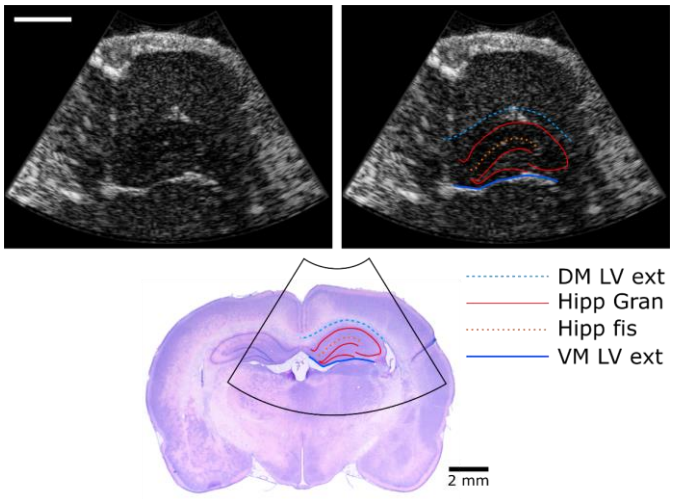


Fig. 3. In vivo rat brain coronal B-mode image (upper left) at *B*−3.0 mm showing the hippocampus. Various layers were identified in the corresponding H&E section (bottom right) and these were overlaid on the B-mode image, showing good correspondence to B-mode features. The lack of white matter HFUS signal is illustrated here, as the corpus callosum white matter (0.5-1.0 mm thick light band above hippocampus in the H&E image, surrounding the DM LV ext) is not distinct in the HFUS image. DM/VM LV ext = dorsomedial/ventromedial extensions of the lateral ventricle, Hipp Gran = hippocampus granular cell layer, Hipp fis = hippocampal fissure.

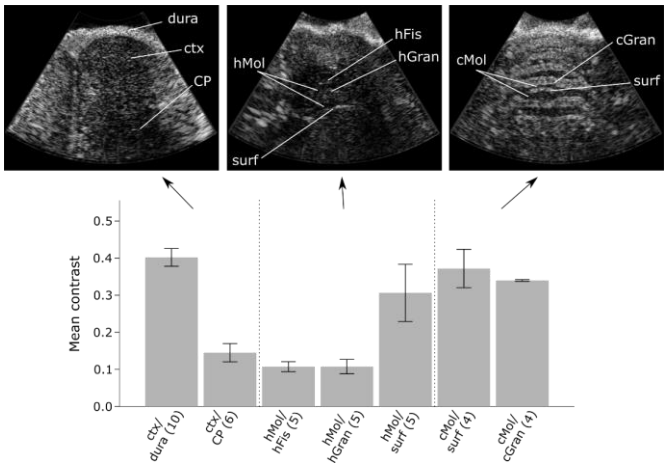


Fig. 4. Contrast values pooled across animals for select tissue comparisons. Examples of the structures are shown in the upper B-mode images. The sample size for each bar is shown in parentheses. cGran = cerebellar granular layer, cMol = cerebellar molecular layer, CP = caudate putamen, ctx= cortex, hFis = hippocampal fissure, hGran = hippocampal granular layer, hMol = hippocampal molecular layer, surf = abutting surface line. Error bars ± 1 SEM.

were typically not very distinct (Figs.2,3). In images captured with the VisualSonics system, the white matter was slightly more visible, most likely due to higher bandwidth and spatial compounding, but not to the degree anticipated.

Human brain samples were notably different in this regard. The white matter was more distinct in both the custom endoscope (Fig.5) and VisualSonics images. When visible, in both rat and human tissue, white matter was darker than gray matter. As with rat brains, a comparison of human cortex brightness before and after dura removal showed no significant

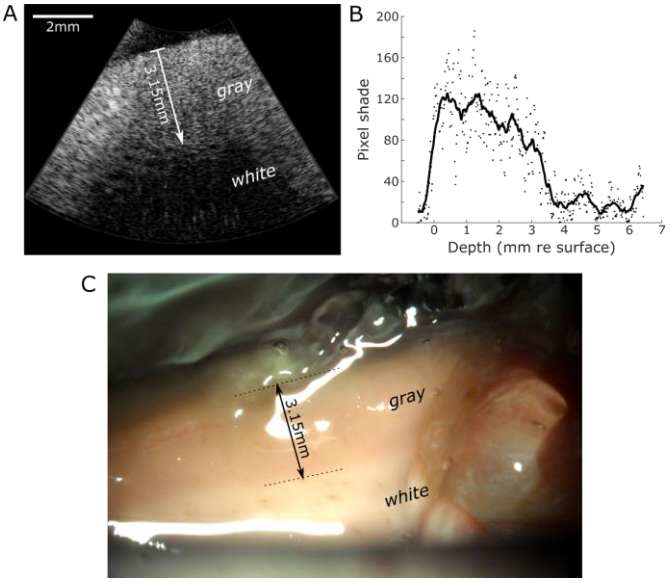


Fig. 5. A) B-mode image of ex vivo human cortex showing the gray matter/white matter contrast. B) B-mode pixel shade values over a line of similar trajectory as the arrow in A. The solid line is a 25-point moving average. C) Photograph of the same brain region dissected to view the tissue appearance. The 3.15 mm gray matter thickness in the tissue agrees with the B-mode data, although the more gradual reduction in B-mode brightness with depth did not correspond to any clear visual transition.

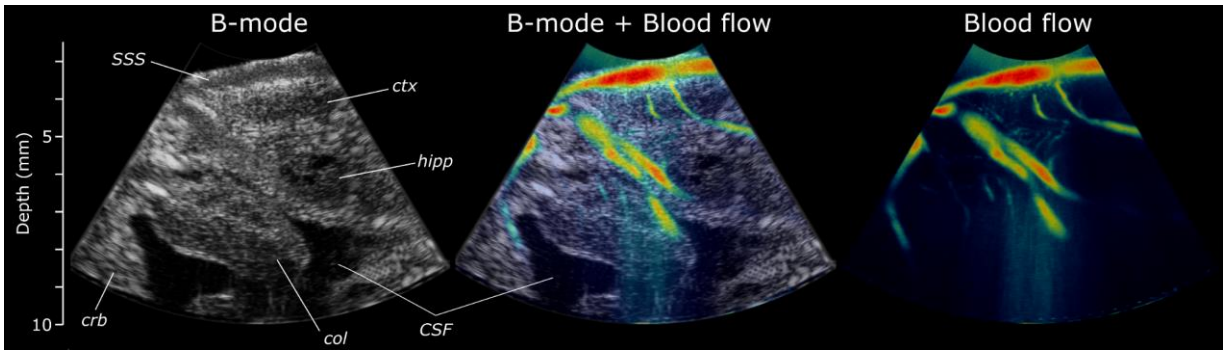


Fig. 6. In vivo rat brain sagittal B-mode image near midline (left) showing many structures. Many blood vessels of a range of diameters were seen in the blood flow image (right; 150 averages). col = colliculus, crb = cerebellum, CSF = cerebrospinal fluid, ctx = cortex, hipp = hippocampus, SSS = superior sagittal sinus.

difference despite the thicker human dura. Imaging the much larger human anatomy with the 45 MHz endoscope was difficult due to limitations of the window size and penetration depth.

In the regular B-mode imaging for both endoscope and VisualSonics images, fast speckle movement could often be easily seen along narrow paths, indicative of blood vessels. These stood out against the much more static speckle pattern of the surrounding brain tissue. The smaller of these vessels almost always appeared brightly in our endoscope blood flow imaging data, as well as some vessels which were not obvious in B-mode imaging. Vessels as small as 50 µm diameter were visible in averaged blood flow data (Fig.6). However, blood flow in large vessels, such as the superior sagittal sinus, appeared with greatly varying intensity between animals, and even within the same vessel within animals.

## IV. Discussion

The imaging results of this study show that various features of brain anatomy can be visible in vivo with HFUS. The most obvious features, other than the distinction at the surface between gel, dura mater, and brain tissue, tended to be boundary between two internal brain surfaces, even where there was no appreciable fluid space between the surfaces.

The consistent lack of contrast in the rat brains between white and gray matter was surprising, although at least part of the reason may be hinted at by the human ex vivo cortex images. The overall contrast between human white and gray matter was substantial (0.36), but the transition in the HFUS image was gradual, spanning about 2 mm (Fig.5B). Brain tissue visually appears to have a more abrupt transition. Therefore, white matter may have been less apparent in rat brains because the boundary in HFUS images may be much less sudden than expected based on visual appearance. The smaller thickness of rat white matter may result in the transition zone effectively occupying the entire white matter region in HFUS images, rendering it less detectable, or at least less sharp.

The imaging window size was limited by the low penetration depth of the high imaging frequency. With regards to visible anatomical features, there turned out to be little advantage to imaging brain tissue at such a high frequency when 30 MHz and 48 MHz images of the same tissue using the VisualSonics system were compared. Furthermore, the low penetration depth limited the extent of visible brain area. In human brains, this limitation is likely to hinder most applications. Therefore, a lower frequency (e.g. 30 MHz) imaging probe and beamformer setup would be more suitable for most applications. We are currently developing 4 mm 30 MHz endoscopes for our system.

The real-time rudimentary power Doppler worked well for some blood vessels but not others. Large vessels in particular were not shown reliably. This is likely a result of using only two power Doppler lines at a relatively high PRF (10 kHz), which relies upon a significant signal change at a given pixel location within the short 100 µs line-to-line sampling interval. This means that low blood flow velocity will be lost in the noise and not be detected. Slower movement within large vessels, therefore, was not reliably detected with the current implementation of firmware/software. Furthermore, the velocity sensitivity range is difficult to determine, as is the actual velocity of a given pixel value because the reported value is dependent upon signal brightness, direction of motion, and actual velocity. We are in the process of implementing ultrafast acquisition which will allow more quantitative Doppler blood flow measurement over a greater range of velocities, among other new capabilities.

## Acknowledgment

For important contributions to the beamformer hardware and software used in this study, we would like to acknowledge Nicholas Campbell, Jeffrey Leadbetter, Chris Samson, Alejandro Villalba, and Zhang Yaoyao.

## References

[1] A. Bezanson, R. Adamson, and J. A. Brown, “Fabrication and performance of a miniaturized 64-element high-frequency endoscopic phased array.,” IEEE Trans. Ultrason. Ferroelectr. Freq. Control, vol. 61, no. 1, pp. 33–43, Jan. 2014.

[2] I. J. Gerard, M. Kersten-oertel, K. Petrecca, D. Sirhan, J. A. Hall, and D. L. Collins, “Brain shift in neuronavigation of brain tumors: A review,” Med. Image Anal., vol. 35, pp. 403–420, 2017.

[3] J. A. Brown, S. Sharma, J. Leadbetter, S. Cochran, and R. Adamson, “Mass-spring matching layers for high-frequency ultrasound transducers: a new technique using vacuum deposition.,” IEEE Trans. Ultrason. Ferroelectr. Freq. Control, vol. 61, no. 11, pp. 1911–21, Nov. 2014.

[4] A. Serrano-pozo, M. P. Frosch, E. Masliah, and B. T. Hyman, “Neuropathological Alterations in Alzheimer Disease,” Cold Spring Harb. Perspect. Med., vol. 1, no. 1, pp. 1–23, 2011.

[5] G. Paxinos and C. Watson, The rat brain in stereotaxic coordinates, 7th ed. Academic Press, 201